


Reversible multielectron transfer I^-/IO_3^- cathode enabled by a hetero-halogen electrolyte for high-energy-density aqueous batteries

Received: 5 March 2023

Accepted: 21 March 2024

Published online: 23 April 2024

 Check for updatesCongxin Xie^{1,4}, Chao Wang^{2,3,4}, Yue Xu^{1,3}, Tianyu Li¹ , Qiang Fu²  & Xianfeng Li¹  

The ever-increasing need for energy-dense batteries with high safety is fuelling global research and innovations in new redox chemistry and device design. Here we show an aqueous battery employing highly concentrated hetero-halogen electrolytes that contain I^- and Br^- , resulting in a multielectron transfer process of I^-/IO_3^- . The intermediate bromide species IBr and Br_2 , generated during the electrochemical process, enhances the reaction kinetics and alleviates the potential gap between oxidation and reduction. When using a 6 M I^- electrolyte to achieve over 30 M electron transfers, the I^-/IO_3^- cathode displayed a high specific capacity of over 840 Ah $I_{\text{catholyte}}^{-1}$. A battery with Cd/Cd^{2+} as the anode demonstrated a high energy density of over 1,200 Wh $I_{\text{catholyte}}^{-1}$. Even at an exceptionally high current density of 120 mA cm^{-2} , an energy efficiency of 72% was obtained. Our work demonstrates that safe aqueous batteries with high energy density are possible, offering a development option for grid-scale energy storage and even electric vehicles.

The ever-increasing energy demand and climate change necessitate the exploration of sustainable energy alternatives, particularly renewable energy. With the wide deployment of renewable energy, batteries are essential for grid-scale electrical energy storage and transport applications. As one of the most important indices for batteries, energy density (Wh kg^{-1} or Wh l^{-1}) describes how much energy a battery contains in proportion to its weight or volume, which in turn indicates how long the battery lasts. Traditional non-aqueous lithium-ion batteries (LIBs) possess high energy density (~ 300 Wh kg^{-1} or 700 Wh l_{cathode}^{-1}) (ref. 1), but their non-aqueous carbonate electrolyte is highly flammable^{2,3}. In contrast, aqueous batteries have the potential to address this issue naturally; however, their energy densities are low (< 200 Wh $I_{\text{catholyte}}^{-1}$) (refs. 4,5), limited by their narrow potential window (~ 2 V vs 5 V

for non-aqueous) and low specific capacity (~ 100 mAh g_{cathode}^{-1} or 170 Ah $I_{\text{catholyte}}^{-1}$), making such batteries compelling only for large-scale stationary energy storage, such as flow batteries.

For a battery, the energy density is mainly determined by the concentration of redox species and the number of electron transfers per molecule. For example, the concentration of Li^+ in the cathode of LIBs, for example, $LiFePO_4$, exceeds 20 M, whereas the concentration of vanadium ions in a vanadium flow battery electrolyte is approximately 2 M. With a fixed concentration, the energy density depends primarily on the number of electron transfers in each mediator molecule. For example, using 0.5 M $P_2W_{18}O_{62}^{6-}$ as a reactant⁶, Conner et al. realized an 18-electron transfer reaction to achieve an energy density of 225 Wh I_{anolyte}^{-1} . Whereas multielectron transfer redox pairs such

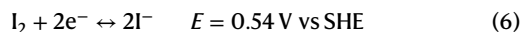
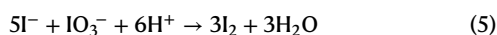
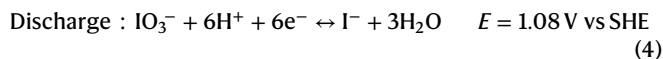
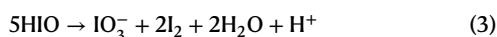
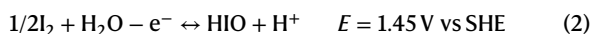
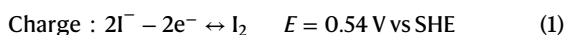
¹Division of Energy Storage, Dalian Institute of Chemical Physics, Chinese Academy of Sciences, Dalian, China. ²State Key Laboratory of Catalysis, iChEM, Dalian Institute of Chemical Physics, Chinese Academy of Sciences, Dalian, China. ³University of Chinese Academy of Sciences, Beijing, China.

⁴These authors contributed equally: Congxin Xie, Chao Wang. ✉e-mail: lixianfeng@dicp.ac.cn

as methyl-viologen⁷ and quinone⁸ are common in organic systems, electron transfer is limited to only two per molecule, further limiting their energy density.

An alternative strategy to achieve high energy density is to combine a high-concentration electrolyte and multielectron transfer reaction. Among the numerous aqueous batteries, the single-electron-transfer iodide/iodine (I^-/I_2) redox couple has been most well studied for use in high-energy-density batteries because it is highly soluble (10 M I^-) and has excellent reversibility and activity^{5,9}. However, the energy density is still much lower than that of LIBs. Nonetheless, in addition to I_2 , the stable high-valence (+5) iodine of iodate (IO_3^-) suggests that a six-electron-transfer process from I^- to I_2 and then to IO_3^- is possible. In addition to the high solubility of I^- (10 M), the theoretical specific capacity for the I^-/IO_3^- couple can reach 1,608 Ah I^- (Supplementary Fig. 1), which is much higher than that of the cathode of LIBs (for example, $LiCoO_2$ - 575 Ah I^-) (refs. 10,11) and comparable to that of lithium metal anode¹² (-2,000 Ah I^-).

However, the problem is that I_2/IO_3^- shows a huge potential gap between oxidation and reduction. During oxidation, I^- is oxidized into I_2 (equation (1)) and then to HIO (equation (2))^{13,14}, followed by disproportionation side reaction to IO_3^- (equation (3))¹⁵. In addition, it is difficult for symmetrical I_2 molecules to expose the positive charge centre and combine with oxygen in H_2O to form HIO, which limits the kinetics. On the contrary, the reduction of IO_3^- , in fact, is a 'self-catalysis' process^{16,17}, through chemical reaction with I^- (equations (4)–(6))^{16–19}, which comes from equation (4) with poor kinetics. The above results indicate that the potential gap between oxidation (I_2/HIO , 1.45 V vs SHE) and reduction (I^-/I_2 , 0.54 V vs SHE) is as high as -910 mV (SHE refers to standard hydrogen electrode potential and E refers to the electrode potential).



In this work, we tuned the electrolyte chemistry by introducing Br^- into the I^- solution. This regulated the reaction process by forming intermediate IBr and Br_2 (Fig. 1a), thereby improving the kinetics of I_2/IO_3^- and reducing the potential gap between oxidation and reduction. For the hetero-halogen electrolyte, during oxidation, after I^- was oxidized to I_2 (step (1)), it subsequently combined with Br^- to form IBr by an electrochemical process (step (2)). This process avoided the formation of unstable HIO and prevented subsequent disproportionation side reactions. Moreover, the high polarity of IBr enabled the positive charge centre to concentrate on the iodine atom, facilitating the nucleophilic attack of H_2O to form $Br_2 + IO_3^-$ (step (3))¹⁴ and thus reducing the oxidation potential and improving the kinetic. For the reduction, Br_2 was reduced to Br^- first, and then Br^- was oxidized by IO_3^- to produce Br_2 and IBr , which continued to participate in reduction (steps (4) and (5)). Because the redox potentials of Br_2/Br^- (1.08 V vs SHE) and IBr/I_2 (1.02 V vs SHE) were closer to that of IO_3^-/IBr (1.20 V vs SHE), the reduction potential was greatly improved.

By using a high-concentration hetero-halogen electrolyte containing I^- and Br^- in a strong acid (denoted as IBA), we realized a multielectron transfer redox in this work. With IBA as the catholyte and

Cd^{2+}/Cd as the anolyte (IBA-C) (Fig. 1b), an energy density of over 1,200 Wh $I_{\text{catholyte}}^{-1}$ or a specific capacity of over 840 Ah $I_{\text{catholyte}}^{-1}$ (Fig. 1d) based on the volume of the catholyte were achieved. Notably, these values exceed that of some solid electrode materials (for example, $LiFePO_4$) (Fig. 1c), enabling the design of high-energy-density aqueous batteries.

Electrochemical testing of electrolytes with and without Br^-

For the electrolyte containing only I^- (IA), cyclic voltammetry (grey curve) was conducted to investigate the electrochemical behaviour in an acidic medium (Fig. 1e). Two oxidation peaks and two reduction peaks in the potential range of 0.8–2.3 V were detected. The oxidation reaction at 1.0 V (step (1)) corresponded to the oxidation of I^- to I_3^- and then to I_2 , while step (2) at -2.0 V was the oxidation of I_2 to HIO ¹⁴, which was rapidly disproportionated into I_2 and HIO_3 ¹⁵. The reduction of HIO only could be observed with a low-concentration electrolyte (10 mM I^-) at high scan rate (50 $mV s^{-1}$) (Supplementary Fig. 2). For the reduction process, step (3) was attributed to the reduction of IO_3^- via I_2/I^- (equations (4)–(6)), which was essentially the same as the I_2 discharge in step (4). The potential of step (3) was higher than that of step (4) (-100 mV higher) because there was a large amount of IO_3^- in step (3), which enabled a low concentration of I^- and then increased the redox potential of I_2/I^- .

For the IBA electrolyte, the cyclic voltammograms (cyan curve) clearly showed six distinct processes (Fig. 1e) in agreement with the mechanism described in Fig. 1a. Compared with IA (step (2) for grey curve), the peak current of IBr to IO_3^- (step (3) for cyan curve) was much higher, which was attributed to fact that polar IBr was more likely to combine with H_2O . The binding energy and the molecular electrostatic potential (ESP) indicated that the interaction between IBr and H_2O was much higher than that of I_2 (Supplementary Fig. 3). Compared with the HBr electrolyte (red curve), IBA showed a more obvious step (4) (Br_2/Br^- i_p , -4 vs -13 mA) due to the chemical–electrochemical discharge of HIO_3 via Br_2/Br^- . Furthermore, step (4) was inhibited as the HBr concentration decreased (0.75 to 0.25 M) (Supplementary Fig. 4) due to the restricted chemical reaction. When the HBr concentration in IBA was increased to 2 M, step (4) dominated and step (5) almost disappeared (Supplementary Fig. 5). IBr exhibited an obvious reduction process (step (5)) regardless of the scan rate or electrolyte concentration (Supplementary Figs. 6–7), which indicated a chemical stability much higher than that of HIO.

The charge–discharge performance of IA and IBA coupled with the Cd^{2+}/Cd anode (Supplementary Fig. 8) is shown in Fig. 1f,g, respectively. At 20 $mA cm^{-2}$, due to the reduction in voltage gap, the voltage efficiency (VE) of the assembled battery with IBA was 19% higher than IA (VE: 82% vs 63%). At 80 $mA cm^{-2}$, IBA showed advantages over IA in terms of capacity and efficiency (78% vs 60%; 184 vs 106 Ah I^-). For the IBA catholyte, by comparing the discharge characteristics of the $Br_2 + IBr$ electrolyte (Supplementary Fig. 9), it was further determined that the discharge mechanism of steps (4) and (5) was the reduction of Br_2 and IBr , respectively. Similarly, steps (3) and (4) of the IA corresponded to the discharge behaviour of HIO_3 (Supplementary Fig. 10a). In addition, the abnormal voltage increase in the initial stage of HIO_3 discharge (Supplementary Fig. 10b) was caused by the reduction of HIO_3 to I^- with poor kinetics (equation (4)), and the generated I^- triggered a 'self-catalysis' process (equations (5) and (6)). Step (2) demonstrated a clear turning point that seemed to be split into two processes (Supplementary Fig. 11). This was because the I_2 generated in step (1) was not conductive, and the layer thickened with deposition time and then detached from the electrode. Step (2) started with priority assigned to the I_2 on the electrode. Afterwards, the I_2 that did not contact the electrode diffused to the electrode only through slight dissolution (the solubility of I_2 was approximately 1 mM) to participate in the charging process.

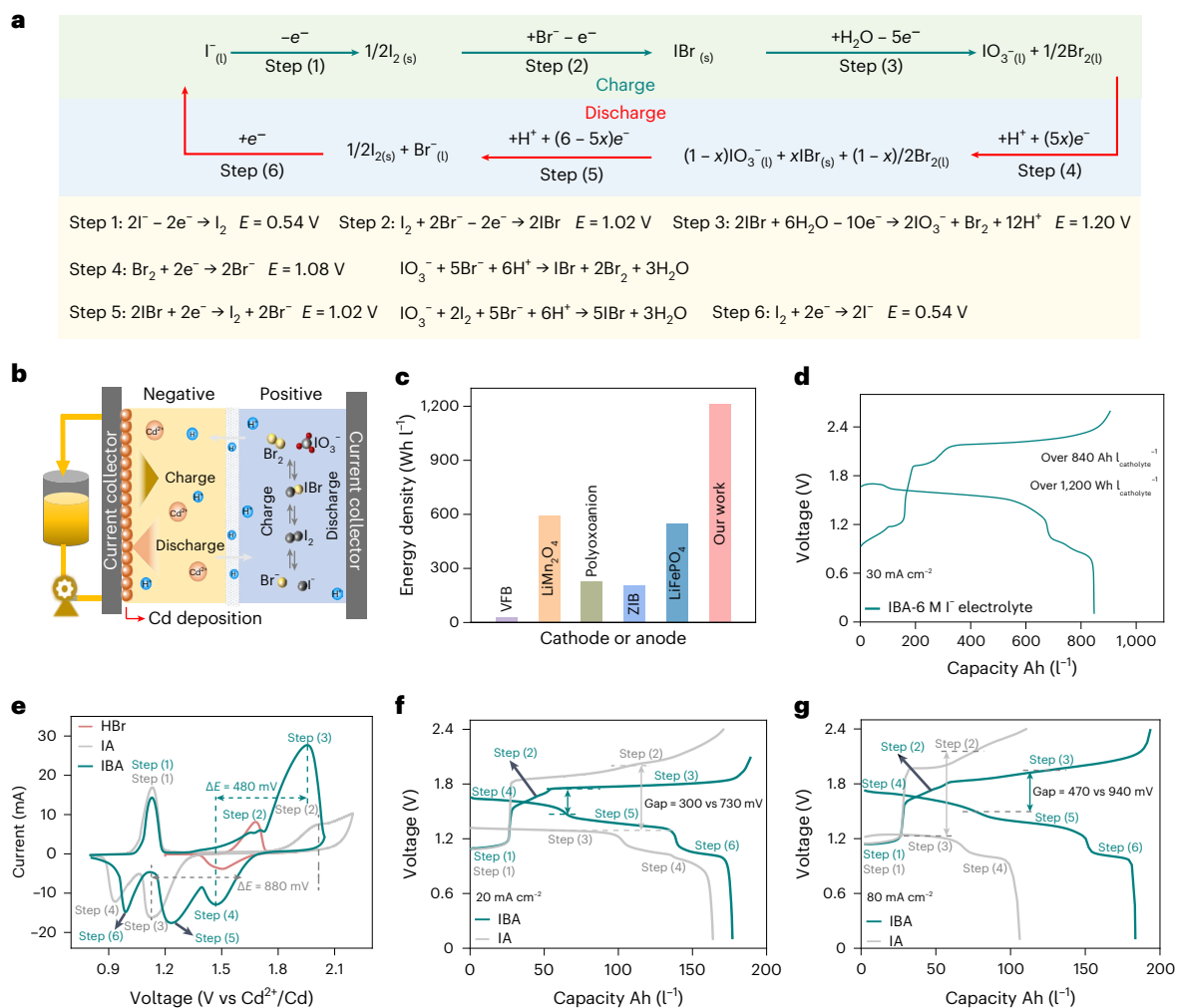


Fig. 1 The multielectron transfer process of IO_3^-/I_2 with or without the addition of Br^- . **a**, Schematic of the charge (steps (1)–(3))–discharge (steps (4)–(6)) process in the presence of Br^- . ‘ x ’ in steps (4)–(5) represents the amount of IO_3^- reduced, and the value is between 0 and 1, which needs to be analysed under specific circumstances. **b**, Schematic of an assembled battery with a multielectron transfer cathode (grey side) and cadmium metal as the anode (yellow side). The electrolyte at the anode flowed, while the electrolyte at the cathode stayed in the electrode cavity. **c**, The energy density of our cathode reached over 1,200 Wh l_{catholyte}⁻¹ (specific capacity over 840 Ah l_{catholyte}⁻¹), far better than that of other cathodes or the anode. All data were calculated from the output energy and the volume of the electrolyte or the solid cathode (calculation details for energy density in the Methods). **d**, Charge–discharge plots of the battery assembled with 6 M Γ in the catholyte. Electrolyte composition:

3 M NaI + 3 M HI + 1 M HBr for catholyte, 1 M CdI₂ + 2 M HBr + 1 M H₂SO₄ for anolyte. **e**, Cyclic voltammogram of IBA (cyan curve), 1 M HBr (red curve) and IA (grey curve) at 1 mV s⁻¹. (IA electrolyte: 1 M HI + 1 M H₂SO₄ + 1 M CdSO₄; IBA electrolyte: 1 M HI + 1 M HBr + 1 M H₂SO₄ + 1 M CdSO₄). Among them, IBA exhibited six charge–discharge steps and IA exhibited four steps. Compared with that of IBA, the reduction current of the electrolyte containing only 1 M HBr (red curve) was much lower, indicating that step (4) involved a chemical–electrochemical process. **f, g**, The charge–discharge curves of the IBA and IA electrolytes at 20 mA cm⁻² and 80 mA cm⁻². Compared with the IA electrolyte, IBA exhibited a lower voltage gap. (IBA electrolyte: 1 M HI + 1 M HBr + 1 M H₂SO₄ + 1 M CdSO₄; IA electrolyte: 1 M HI + 1 M H₂SO₄ + 1 M CdSO₄). The battery details are provided in Supplementary Tables 2–4.

Electrochemical mechanism of the hetero-halogen electrolyte

To verify the possibility of the multielectron transfer mechanism of IBA, we began with ex situ characterization to simulate the formation of IBr in step (2) by mixing I_{2(s)} with Br_{2(l)} at different molar ratios. The Raman (214 cm⁻¹) (refs. 20–22) and ultraviolet (253 nm) (ref. 23) spectra confirmed the formation of IBr (Fig. 2a and Supplementary Fig. 12). At high molar ratios of Br₂ to I₂ (>2:1), the generated IBr dissolved in excess Br₂ and formed a homogeneous and stable solution (Supplementary Fig. 13a). At low ratios, I₂ precipitates were clearly observed (Supplementary Fig. 13b,c). Furthermore, IBr also rapidly dissolved in a 1:1 mixture of IBr and Br₂ (Supplementary Fig. 13d). These results confirm the charging-formed IBr as outlined in step (2) (Fig. 1a).

We also simulated the reduction process of IO_3^- during discharge by mixing HIO₃ and HBr at different molar ratios. The Raman spectra

showed that IO_3^- easily oxidized Br^- into Br₂ and IBr (Fig. 2b), according to the chemical–electrochemical process outlined in steps (4) and (5). Simulated electrolytes composed of different ratios of HI to HIO₃ demonstrated that as the battery discharged, IBr precipitated from Br₂ to form deposits on the electrode that triggered step (5) (Supplementary Fig. 14).

To confirm these ex situ observations, we used in situ Raman spectroscopy (Fig. 2c) and X-ray diffraction (XRD) (Fig. 2d) to follow the multielectron transfer chemistry of IBA. During initial charging, we observed an I₂ signal from step 1 at 180 cm⁻¹ (refs. 24,25) and an I₃⁻ signal at 112 cm⁻¹ (Supplementary Fig. 15a)²⁶. Further charging resulted in the appearance of a new peak at 219 cm⁻¹, which was assigned to the stretching vibration of I–Br^{20–22}. Strong peaks at 300–400 cm⁻¹ and 700–800 cm⁻¹ were attributed to the formation of IO_3^- in step (3)^{27,28}. The formed IO_3^- precipitated with Cd²⁺ to form Cd(IO₃)₂ ($K_{sp} = 2.5 \times 10^{-8}$)

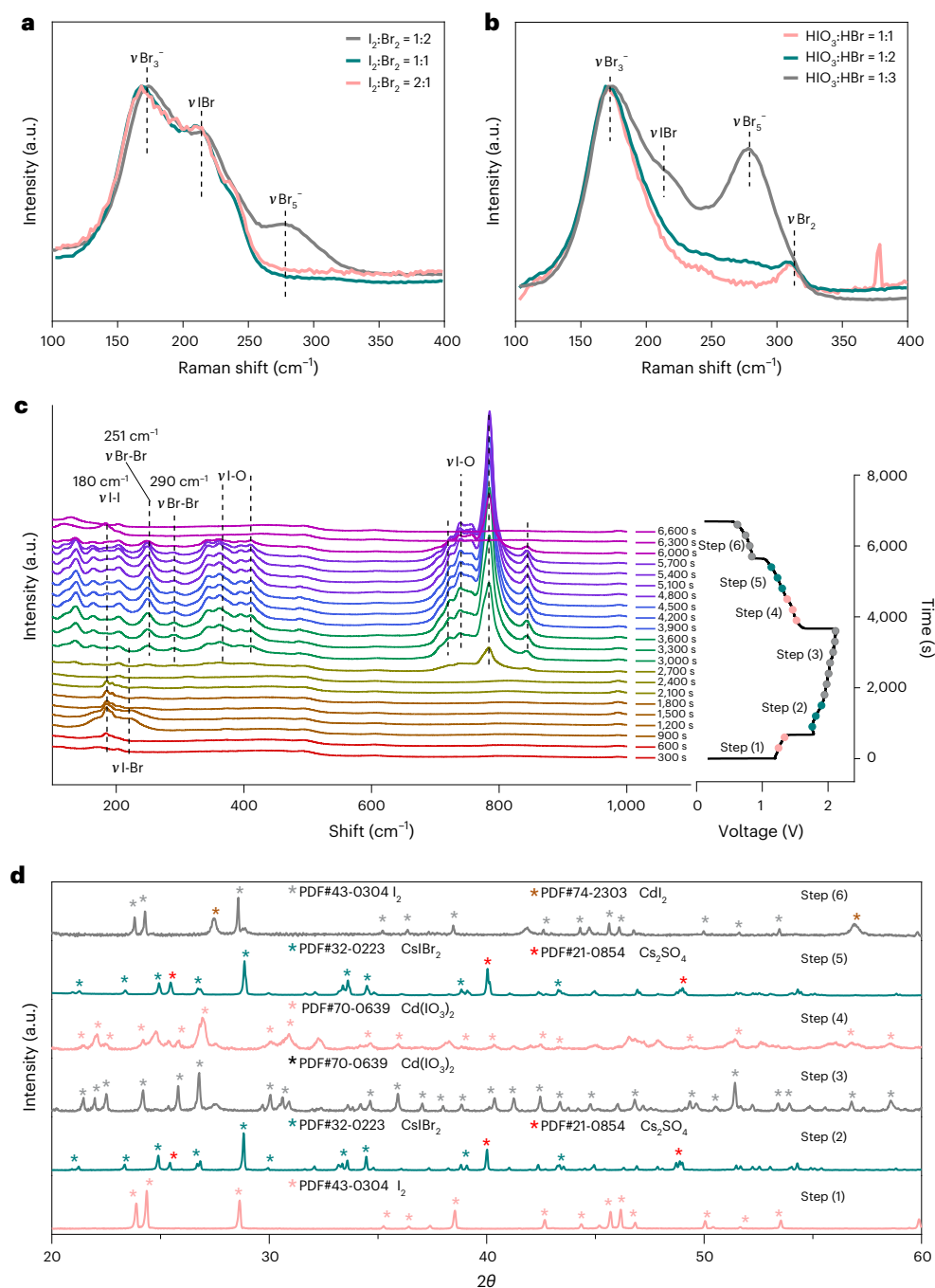


Fig. 2 | Characterization of multielectron transfer of halogen electrolytes

IBA. a. Raman spectra of mixed solutions of $I_{2(s)}$ and Br_{20} at different molar ratios. The Raman vibration signals were assigned to $I-Br$ (214 cm^{-1}), Br_3^- (168 cm^{-1}) and Br_5^- (278 cm^{-1}). The formation of Br_{2n+1}^- followed equations (1)–(3); equation (1): $I_2 + Br_2 \rightleftharpoons 2IBr$; (hydrolysis) equation (2): $Br_2 + H_2O \rightleftharpoons HBrO + HBr$; equation (3): $HBr + nBr_2 \rightleftharpoons HBr_{2n+1}$. **b.** Raman spectra of mixed solutions of HIO_3 and HBr at different molar ratios. The signals for Br_3^- and Br_2 in the 1:1 and 1:2 solutions indicated that IO_3^- could easily oxidize Br^- . At higher proportions of HBr ($HIO_3:HBr = 1:3$), the $I-Br$ signal was observed. **c, d.** In situ Raman spectra

($100\text{--}1,000\text{ cm}^{-1}$, left) and the corresponding charge–discharge plot (right) of IBA (**c**) and ex situ XRD spectra of the products from each step (**d**). All steps in **c** corresponding to the Raman curves are marked with coloured points in the charge–discharge plot. The vertical dotted lines in **c** indicate vibrational modes of Raman signals. The Raman spectra were recorded every 100 seconds. XRD spectra were obtained in the 2θ range of $20\text{--}60^\circ$. Scan mode (θ , diffraction angle) was applied with $Cu\ K\alpha$ radiation at a wavelength of 1.5418 \AA . Electrolyte composition in **c** and **d**: $1\text{ M HI} + 1\text{ M HBr} + 1\text{ M H}_2\text{SO}_4 + 1\text{ M CdSO}_4$.

(Supplementary Fig. 16). Moreover, the signals at 162 cm^{-1} and 290 cm^{-1} were assigned to the polyhalogens of Br_3^- (ref. 29) and Br_{11}^- (refs. 30,31), respectively (Fig. 2c and Supplementary Fig. 15b). In addition, the signal at 311 cm^{-1} was attributed to Br_2 (Supplementary Fig. 15b)³². Following discharge, signals for IO_3^- and Br_{11}^- corresponding to the chemical–electrochemical processes (steps 4) and (5) were clearly observed. The signal of $I-Br$ in step (5) was further confirmed by ex situ

Raman spectroscopy (Supplementary Fig. 17) because it was overlaid with $Cd(IO_3)_2$ during the in situ process. The disappearance of the I_2 signal confirmed step (6). XRD analysis of the products from each of the six steps corroborated the presence of key compounds (Fig. 2d). Importantly, the XRD signal of $I-Br$ was strengthened by introducing Cs^+ into the solution to precipitate $CsI-Br_2$ in steps (2) and (5) (Supplementary Fig. 18 and Fig. 2d).

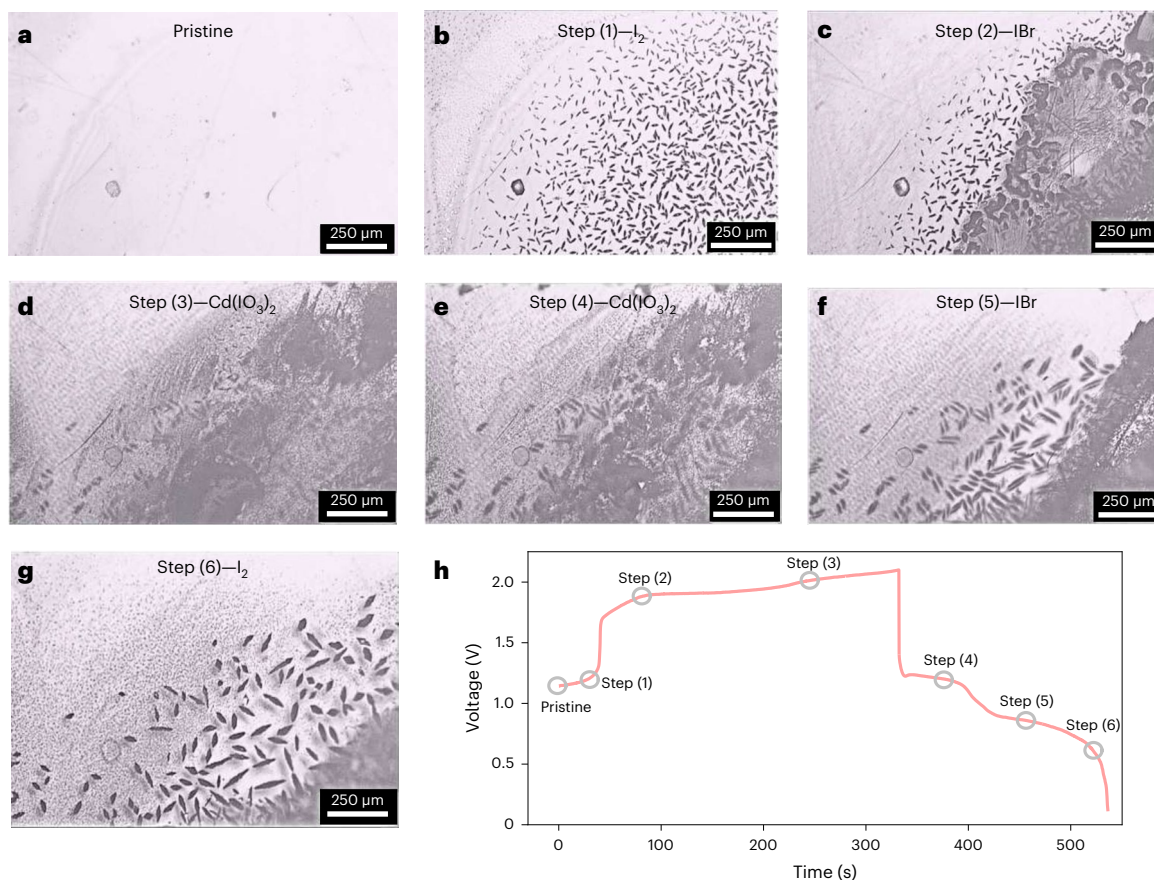


Fig. 3 | In situ observation of the charge–discharge process of IBA under an optical microscope. **a–g**, Optical microscopy images of the electrode surface morphology at different charge and discharge stages: pristine (**a**),

step (1) (**b**), step (2) (**c**), step (3) (**d**), step (4) (**e**), step (5) (**f**) and step (6) (**g**). **h**, The corresponding charge–discharge plot. Electrolyte composition: 1 M HI + 1 M HBr + 1 M H₂SO₄ + 1 M CdSO₄.

We also inspected the charge–discharge process with an in situ microscope (Fig. 3 and Supplementary Video 1). During initial charging (step (1)), spindle-shaped I₂ particles were clearly seen on the electrode (Fig. 3b). Oil droplets that formed upon further charging (step (2)) indicated the presence of IBr (Fig. 3c). In step (3), most of the IBr droplets were converted into a mist of Cd(IO₃)₂ that covered the electrode surface (Fig. 3d). Upon discharge, the misty Cd(IO₃)₂ gradually disappeared, and the spindle-shaped I₂ was regenerated (steps (4) and (5)) (Fig. 3e,f) (IBr was overlaid with Cd(IO₃)₂). At the end of discharge (Fig. 3g), I₂ particles gradually dissolved.

In contrast to IBA, we also studied the electrochemical mechanism of IA without Br[−] by in situ Raman spectroscopy (Supplementary Fig. 19) and ex situ XRD (Supplementary Fig. 20). Consistent with the literature, Raman signals of I₂ (180 cm^{−1}) (refs. 24–25) and IO₃[−] (300–400 cm^{−1} and 700–800 cm^{−1}) (refs. 27,28) were observed upon charging in steps (1) and (2), respectively. Due to the unstable HIO, it was difficult to observe signals for this species. During discharging in step (3), the IO₃[−] signal gradually weakened, while the intensity of I₂ increased, indicating the gradual conversion of IO₃[−] to I₂. Upon further discharging in step (4), I₂ was completely reduced to I[−], as shown by the disappearance of the I₂ signal. In situ microscopy confirmed this process as well (Supplementary Fig. 21 and Supplementary Video 2). The XRD spectra of the products in each step were also consistent with the in situ Raman data.

Battery performance with a hetero-halogen electrolyte

To demonstrate the feasibility of IBA, we assembled a single flow battery with IBA as the catholyte and Cd/Cd²⁺ as the anode (IBA-C)

(Supplementary Fig. 22). The battery demonstrated six steps, and changes in the electrolyte at each step were visually observed in optical photographs (Fig. 4a). The anode was used as the flow mode to prevent dendrite formation in Cd plating/stripping. Polarization curves for various states of charge (SOC) of IBA-C showed that when the SOC was 90%, the peak power density reached 474 mW cm^{−2} at a current density of 640 mA cm^{−2} (Supplementary Fig. 23). The energy efficiency decreased from 82% to 63% as the current density increased from 20 to 160 mA cm^{−1} (Fig. 4b and Supplementary Fig. 24). Even at a high current density of 120 mA cm^{−2}, an energy efficiency of 72% was obtained. Compared with the energy density of the battery with IA, at 80 mA cm^{−2}, the energy density of IBA was two times higher (260 vs 119 Wh I_{catholyte}^{−1}) due to its higher discharge voltage and specific capacity (184 vs 106 Ah I_{catholyte}^{−1}) (Supplementary Fig. 25a,b,d,e). Furthermore, the energy efficiency of IBA-C reached 75% (vs 58% for IA) (Supplementary Fig. 25c,f). Increasing the I[−] concentration in IBA from 1 M to 6 M, the energy density increased from 260 to over 1,200 Wh I_{catholyte}^{−1} (Fig. 4c and Supplementary Fig. 26), and the electron transfer concentration reached over 30 M (Supplementary Fig. 27). However, as the electrolyte concentration increased, the power density of the battery decreased (Supplementary Fig. 26; 80 mA cm^{−2} at low concentrations (IBA-2 - 3 M I[−] electrolyte) vs 30 mA cm^{−2} at high concentrations (IBA-4 - 6 M I[−] electrolyte)). The viscosity test of the electrolyte showed that with increasing concentration, the viscosity of the electrolyte did not increase significantly (Supplementary Fig. 28). The main reason for the decrease in performance was the limited proton concentration in the supporting electrolyte of a higher-concentration electrolyte. Using a high-concentration anolyte (4.5 M CdCl₂) with a 6 M I[−] catholyte, an energy density (based on catholyte + anolyte) of ~185 Wh I_{catholyte+anolyte}^{−1}

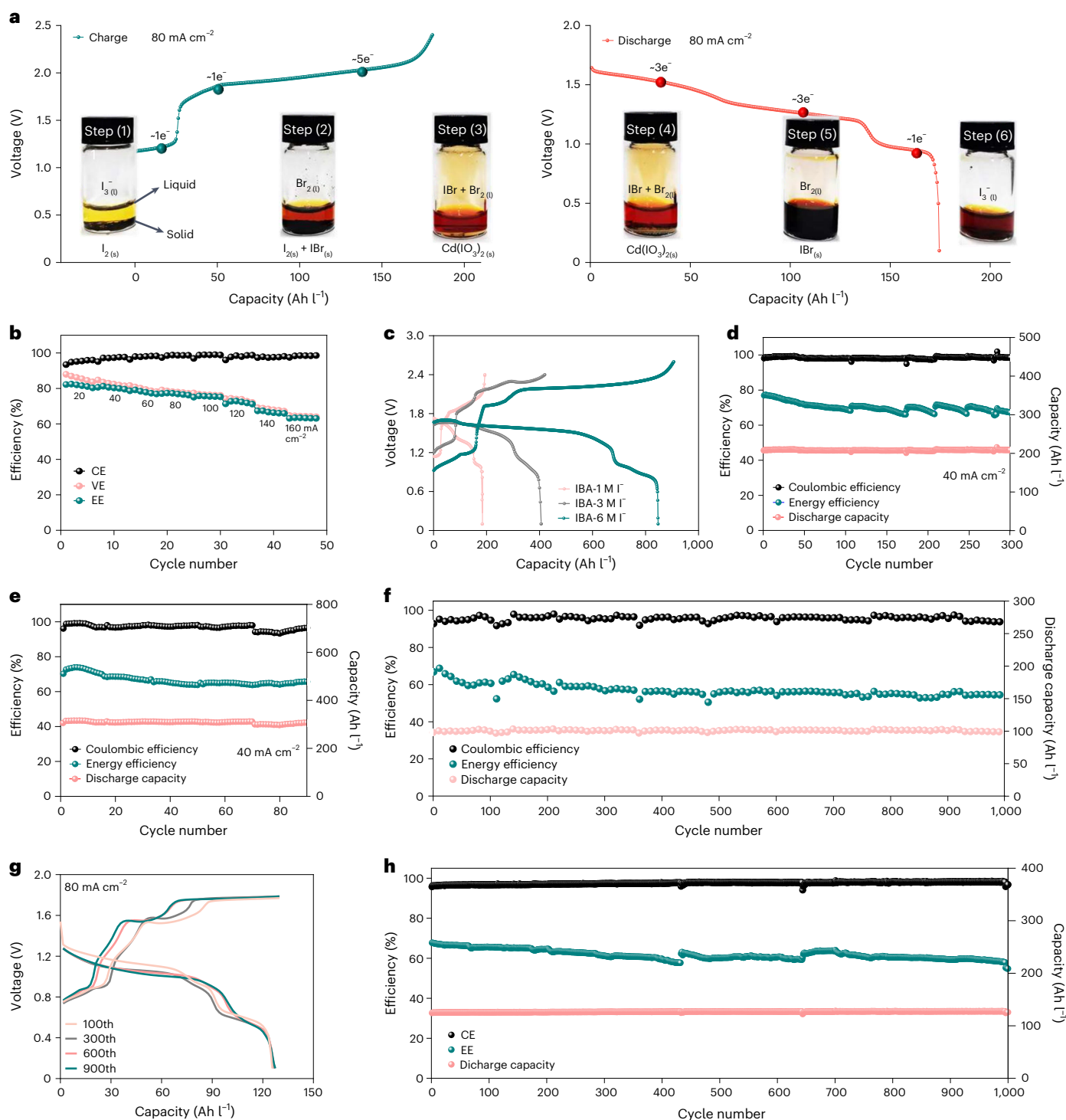


Fig. 4 | Performance of a single flow aqueous battery using IBA as the catholyte and Cd/Cd²⁺, silicotungstic acid or V²⁺/V³⁺ as the anode.

a, Photographs of the electrolyte and their corresponding charge–discharge plots at different steps. Electrolyte composition: 1 M HI + 1 M HBr + 1 M H₂SO₄ + 1 M CdSO₄. **b**, Battery efficiencies at current densities of 20–160 mA cm⁻² with cut-off voltages of 2.1 V and 0.1 V. Electrolyte composition: 0.5 M CdI₂ + 1 M HBr + 3 M H₂SO₄. **c**, Charge–discharge plots of the battery assembled with different concentrations of I⁻ in the IBA catholyte. **d,e**, Cycling performance of the battery with 2 M I⁻ (1 M CdI₂ + 2 M HBr + 3 M H₂SO₄) (**d**) and 3 M I⁻ electrolytes (1 M NaI + 1 M CdI₂ + 2 M HBr + 3 M H₂SO₄) (**e**) at 40 mA cm⁻². The constant capacity for charge limits was 8 M or 12 M electron transfers for the 2 M or 3 M I⁻ electrolytes, respectively, and the discharge voltage cut-off was 0.1 V. **f**, Cycling performance of the IBA-SWO battery at 80 mA cm⁻². Both the catholyte and

analyte were 1 M HI + 1 M HBr + 0.5 M SWO. Fluctuations in the efficiency data were due to water migration and required periodic electrolyte mixing to recover. The constant capacity for the charge limit was -4 M electron transfer, and the discharge voltage cut-off was 0.1 V. **g,h**, The charge–discharge curves (**g**) and cycle performance (**h**) of the assembled battery with V²⁺/V³⁺ as an anolyte at 80 mA cm⁻². Electrolyte composition: 1 M HI + 1 M HBr + 1.5 M H₂SO₄ + 0.4 M VSO₄ + 0.2 M V₂(SO₄)₃. The fluctuation in performance was caused by the migration of the electrolyte and the oxidation of V²⁺ by air, which needed to be restored periodically. The constant capacity for the charge limit was 5 M electron transfer, and the discharge voltage cut-off was 0.1 V. The details of the battery, including the volume of electrolyte, charge and discharge capacity, energy and other data, are provided in Supplementary Tables 2–4.

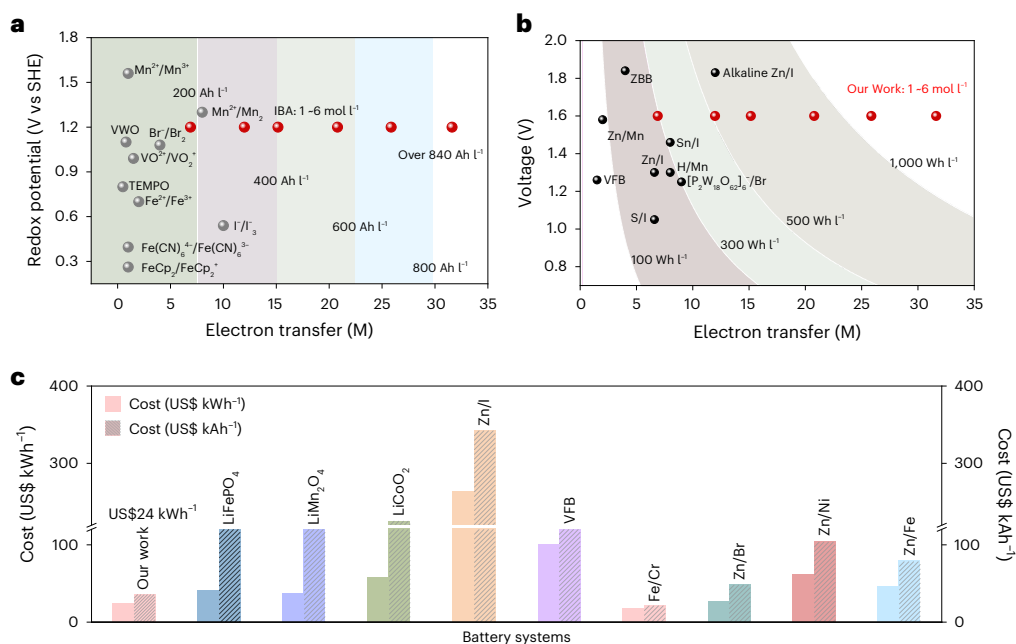


Fig. 5 | IBA-based batteries outperform current battery systems.

a, b, Comparison of the specific capacity and energy density between the IBA-based catholyte and other aqueous systems. The electron transfer number and redox potential in **a** were obtained from the following references: $\text{Mn}^{2+}/\text{Mn}^{3+}$ (ref. 52), $\text{MnO}_2/\text{Mn}^{2+}$ (ref. 53), VWO^{54} , Br^-/Br_2 (ref. 55), TEMPO^{56} , $\text{Fe}^{2+}/\text{Fe}^{3+}$ (ref. 57), I^-/I_3^- (ref. 5), $\text{Fe}(\text{CN})_6^{4-}/\text{Fe}(\text{CN})_6^{3-}$ (ref. 58), $\text{FeCp}_2/\text{FeCp}_2^+$ (ref. 59). The electron transfer number and voltage in **b** were obtained from the following references: tin-iodine flow battery (Sn-I)⁶⁰, zinc-iodine flow battery (Zn-I)²⁶, alkaline zinc-iodine flow battery (alkaline Zn-I)⁶¹, hydrogen-manganese battery (H-Mn)⁵³,

sulfur-iodine flow battery (S-I)⁶², zinc-manganese flow battery (Zn-Mn)⁶³, polyoxoanion-bromine flow battery (PWO-Br)⁶ and zinc bromine flow battery (ZBB)⁶⁴. **c**, Compared with common aqueous and non-aqueous positive electrodes, the cost of our cathode (US\$24 kWh_{cathode}⁻¹, US\$35 kWh_{cathode}⁻¹) was lower than most common aqueous systems, including that based on LiFePO_4 (-US\$41 kWh_{cathode}⁻¹, US\$139 kWh_{cathode}⁻¹) or LiMn_2O_4 (-US\$37 kWh_{cathode}⁻¹, US\$151 kWh_{cathode}⁻¹) in LIBs. The y axis break is 120–220 to better illustrate the histogram of many low-cost systems. Supplementary Table 1 provides the cost calculation (US\$ kWh⁻¹ or US\$ kWh⁻¹) of different positive electrode materials.

was obtained (Supplementary Fig. 29). These results show that IBA is a very promising catholyte for high-energy-density battery design.

Discharge capacity through intermediates of Br_2 and IBr

We also evaluated the performance of batteries assembled with IBA containing different concentrations of HBr . By increasing the Br^- to I^- ratios from 1:1 (1 M HBr :1 M HI) to 3:1 (3 M HBr :1 M HI), we found that the capacity contributed by step (2) increased from -29 to -82 Ah $\text{I}_{\text{catholyte}}^{-1}$, and it increased almost linearly with the amount of Br^- (Supplementary Fig. 30a). In step (2), I_2 and Br^- preferentially formed IBr , and excess Br^- was oxidized to form Br_2 . However, during discharge, we found that as the Br^- to I^- ratios increased from 1:1 to 3:1, the discharge capacity of step (4) gradually increased from -78 to -172 Ah $\text{I}_{\text{catholyte}}^{-1}$, whereas that of step (5) gradually decreased from -70 to -27 Ah $\text{I}_{\text{catholyte}}^{-1}$ (Supplementary Fig. 30b). Because step (5) started with the precipitation of $\text{IBr}_{(s)}$ from $\text{Br}_{2(l)}$, higher ratios of Br^- to I^- generated more Br_2 in the electrolyte. The excess Br_2 dissolved IBr and delayed step (5). As a result, the capacity contributed by step (4) increased, while that contributed by step (5) decreased. For the electrolyte with the same concentrations of Br^- and different concentrations of I^- , the capacities of step (4) were almost constant, while the capacities of step (5) were obviously increased, which also proved the above conclusion (Supplementary Fig. 31). By employing IBr dissolved in Br_2 as the electrolyte, the abnormally short step (4) also resulted from the precipitation of IBr , which triggered step (5) (Supplementary Fig. 32).

Cycling stability of IBA-based batteries

Battery cycle tests showed that IBA was highly stable. At a current density of 40 mA cm^{-2} , IBA-C with 2 M I^- ran continuously for more than 300 cycles, with an energy efficiency 78% and a specific capacity of

210 Ah $\text{I}_{\text{catholyte}}^{-1}$ (Fig. 4d and Supplementary Fig. 33a–c). By increasing the I^- concentration in IBA to 3 M, more than 90 cycles were completed, with an energy efficiency of 74% and a specific capacity of 315 Ah $\text{I}_{\text{catholyte}}^{-1}$ (Fig. 4e and Supplementary Fig. 33d–f). When the current density increased to 80 mA cm^{-2} , the cycle stability decreased to 100 cycles (Supplementary Fig. 34). When the 6 M I^- electrolyte was used, the electrolyte maintained an electron transfer number of -26 M, which allowed it to run stably for more than 20 cycles, and the energy density reached over 850 Wh $\text{I}_{\text{catholyte}}^{-1}$ (Supplementary Fig. 35). The main reason for the limited cycling life was that uneven cadmium plating caused a short circuit (Supplementary Fig. 36).

We also investigated the stability of our IBA catholyte by pairing it with silicotungstic acid (SWO) (IBA-SWO) and $\text{V}^{2+}/\text{V}^{3+}$ (IBA-V). The SWO³³ and $\text{V}^{2+}/\text{V}^{3+}$ anodes demonstrated good electrochemical reversibility and were free of dendrites (Supplementary Fig. 37). As a result, both the IBA-SWO and IBA-V batteries operated stably for more than 1,000 cycles at a current density of 80 mA cm^{-2} (Fig. 4f–h, and Supplementary Figs. 38–40), demonstrating very impressive cycling stability. Increasing the volume of catholyte (-8 ml vs -1 ml), the battery still showed good performance and cycle stability (Supplementary Fig. 41). To reduce the concentration of free Br_2 in the electrolyte, choline chloride was added to the electrolyte as an additive, and the battery could also run stably for more than 400 cycles (Supplementary Fig. 42).

Potential cost efficiency

Our IBA-C battery demonstrated a high specific capacity of over 840 Ah $\text{I}_{\text{catholyte}}^{-1}$, which was much higher than those reported aqueous redox pairs. (Fig. 5a). Furthermore, its energy density of over 1,200 Wh $\text{I}_{\text{catholyte}}^{-1}$ was much higher than that of the current reported aqueous batteries (Fig. 5b), including many plating/stripping-based systems such as Sn^{4+}/Sn or $\text{MnO}_2/\text{Mn}^{2+}$. Most importantly, the realization of

multielectron transfer with IO_3^-/I^- meant that the amount of I^- required per kWh was significantly lower than the I^-/I_2 with a single electron transfer reaction. From our calculation (Methods and Supplementary Table 1), this design decreased the cost to $-\text{US}\$24 \text{ kWh}_{\text{catholyte}}^{-1}$ or $-\text{US}\$35 \text{ kWh}_{\text{cathode}}^{-1}$, comparable to that of the LiFePO_4 cathode in LIBs ($-\text{US}\$41 \text{ kWh}_{\text{catholyte}}^{-1}$ or $\text{US}\$139 \text{ kWh}_{\text{cathode}}^{-1}$) (Fig. 5c). We expect the iodine multielectron transfer system to broaden the application of aqueous batteries.

Conclusions

We developed a high-energy-density aqueous battery system using a highly concentrated hetero-halogen-based electrolyte. By introducing Br^- into the I^- solution, we achieved a reversible multielectron transfer reaction in the I_2/IO_3^- couple. Leveraging the advantages of high electrolyte concentration and multielectron transfer process, the energy density of our catholyte reached over $1,200 \text{ Wh l}_{\text{catholyte}}^{-1}$ with Cd^{2+}/Cd as the anode. Even at a high current density of 120 mA cm^{-2} , the battery had an energy efficiency of 72%. The cycle life of silicotungstic acid or $\text{V}^{2+}/\text{V}^{3+}$ as anode was extended to over 1,000 cycles, demonstrating significant stability. With its high energy density, power density and stability, our multielectron transfer battery system shows promising potential for the development of next-generation high-energy-density and safe rechargeable aqueous batteries.

Methods

Preparation of electrolytes

For the IBA electrolytes, IBA-1 M I^- electrolyte referred to 1 M HI (Sinopharm Chemical Reagent) + 1 M HBr (Tianjin Kemiu Chemical Reagent) + $1 \text{ M H}_2\text{SO}_4$ (DAMA Chemical Reagent) + 1 M CdSO_4 (Aladdin Reagent), and IBA-2 M I^- electrolyte referred to 1 M CdI_2 (Sinopharm Chemical Reagent) + 2 M HBr + $3 \text{ M H}_2\text{SO}_4$. The composition of the IBA-3 M I^- electrolyte was optimized as 1 M CdI_2 + 1 M NaI (Sinopharm Chemical Reagent) + 2 M HBr + $3 \text{ M H}_2\text{SO}_4$. For the IBA-4 - 6 M I^- electrolyte, to obtain the highest solubility, the catholyte compositions were 4 M NaI + 1 M HBr , 3 M NaI + 2 M HI + 1 M HBr and 3 M NaI + 3 M HI + 1 M HBr , respectively, and the anolyte was 1 M CdI_2 + 2 M HBr + $1 \text{ M H}_2\text{SO}_4$. For the IA electrolyte without HBr, IA-1 M I^- electrolyte referred to 1 M HI + $1 \text{ M H}_2\text{SO}_4$ + 1 M CdSO_4 . For the battery performance with $\text{V}^{2+}/\text{V}^{3+}$ as anolyte (-0.4 M V^{2+} + -0.4 M V^{3+}), the mixture of $\text{V}^{2+}/\text{V}^{3+}$ anolyte was obtained by electrolysis ($0.4 \text{ M V}_2(\text{SO}_4)_3$ + 0.8 M VO_2 + $3 \text{ M H}_2\text{SO}_4$), which was employed for vanadium redox flow battery. Supplementary Table 2 provides detailed electrolyte composition.

Cyclic voltammetry test

The cyclic voltammetry test was performed by using a typical three-electrode device with a compressed sandwich structure in which the working electrode was carbon felt (Liaoyang J-Carbon Materials Co.) with a radius of 3 mm, and the counter electrode and reference electrode were 9 cm^2 ($3 \text{ cm} \times 3 \text{ cm}$) cadmium plates (Tianjin Xinjia Weiye Steel Trade Co.). The electrolyte was dropped on carbon felt for electrochemical evaluation. A Nafion 115 membrane was used to separate the working and reference electrodes. The cyclic voltammetry test was performed by means of a Gamry Interface 1000 at scan rates from 1 to 50 mV s^{-1} at room temperature.

In situ Raman spectra

In situ Raman spectra testing included a combination of Raman and electrochemical detection. The assembled battery was charged and discharged through an electrochemical workstation with a constant current of 10 mA. The positive and negative electrodes of the evaluated battery were carbon felts with areas of 0.25 cm^2 ($0.5 \text{ cm} \times 0.5 \text{ cm}$) and 1 cm^2 ($1 \text{ cm} \times 1 \text{ cm}$), respectively. The homemade in situ test device was shown in Supplementary Fig. 43. The battery was assembled with a Nafion 115 membrane with the electrolyte stored inside the porous carbon felt, which was connected to the electrochemical workstation

by titanium wires. The Raman signal was collected from the positive electrode surface under the quartz window, which was recorded by a LabRAM HR 800 Raman spectrometer with a 532 nm laser. The Raman scanning range was $100\text{--}1,000 \text{ cm}^{-1}$, and the signal was collected every 100 s.

Ex situ Raman spectra

For ex situ Raman spectra measurement, the test solution was contained in a nuclear magnetic tube. The Raman spectra were measured by an inVia microscope (Leica) and Raman spectroscopy system (Renishaw). A diode-pumped solid-state laser (532 nm) was used as the excitation source. The scanning range was $50\text{--}1,000 \text{ cm}^{-1}$ at room temperature.

In situ optical microscopy

In situ optical microscopy detection was carried out by using a homemade electrochemical device. A glassy carbon electrode with a size of $1 \text{ cm} \times 1 \text{ cm}$ and a piece of Cd plate ($1 \text{ cm} \times 1 \text{ cm}$) with a thickness of 1 mm served as the positive and negative electrodes, respectively. A piece of Nafion 212 was used as the membrane. Compared with Nafion 115, Nafion 212 is thinner, making it conducive to the construction of the homemade device. The battery was charged and discharged via an electrochemical workstation (LANHE) at a current of 2 mA. An optical microscope (Leica microsystems CMS GmbH) was used to detect the change in surface morphology of the electrode.

XRD determination

XRD detection was performed to detect the product composition on the electrode when the battery was charged or discharged to a certain state. The electrode products were sealed by a piece of polyimide (PI) film to inhibit the volatilization of Br_2 . XRD detection was performed by means of a Rigaku Ultima IV equipped with a D/teX-Ultra detector and $\text{Cu K}\alpha$ radiation from 20 to 60° , and the scanning rate was 10° per minute.

Battery assembly

The battery assembly was similar to that described in our previous articles³⁴. To inhibit the corrosion of Br_2 , a titanium plate (1 mm) and a graphite plate were used as positive and negative current collectors, respectively. Graphite felt (size: $6 \text{ cm} \times 8 \text{ cm}$) with a thickness of 1 mm was used as the electrode (the electrode with the size of $3 \text{ cm} \times 3 \text{ cm}$ was assembled with $\text{V}^{2+}/\text{V}^{3+}$ (Fig. 4g,h) as an anolyte, due to the low concentration of $\text{V}^{2+}/\text{V}^{3+}$ with a compression rate of $\sim 50\%$). In addition, a cadmium plate with a thickness of 1 mm was placed on the negative side to ensure full discharge. The positive and negative electrodes were separated by a piece of Nafion 115. Importantly, the electrolyte on the negative side was in flowing mode to prevent dendrite issues, whereas the electrolyte on the positive side was stored in the positive carbon felt. For the cycling test, a glass fibre separator (AGM Zaozhuang Dongchang Fibreglass Industry Co.) with a thickness of 1.6 mm was placed between the negative electrode and membrane to prevent the short circuit caused by cadmium dendrites.

Battery performance evaluation

For the single-cell performance, the battery was charged/discharged by using a constant current mode with voltage cut-off. The upper limit was 2.4 V, and the lower limit was -0.1 V , as shown in Figs. 1g and 4a,c. For the highest catholyte concentration of 6 M I^- , the upper limit was further raised to 2.6 V, and the lower limit was -0.1 V , as shown in Fig. 1c. For the cycling performance test, the charging cut-off was constant capacity, such as Fig. 4d,e with a constant capacity of 8 M and 12 M electron transfer and 4g,h with a constant capacity of 5 M electron transfer, and a voltage cut-off of -0.1 V was used for discharge. A single-flow battery was assembled, where the catholyte was sealed in the porous positive electrode and an anolyte flowed through the anode.

For the specific capacity and energy density of the battery, they could be obtained by dividing the actual discharge capacity and energy of the battery by the volume of the catholyte.

$$Q_s = \frac{Q_{\text{discharge}}}{V_c} \quad (7)$$

$$E_s = \frac{E_{\text{discharge}}}{V_c} \quad (8)$$

Where Q_s is the specific capacity of the battery (Ah l^{-1}), $Q_{\text{discharge}}$ is the actual discharge capacity of the battery (Ah), V_c is the volume of the catholyte (l); E_s is the discharge energy density of the battery (Wh l^{-1}), $E_{\text{discharge}}$ is the actual discharge energy of the battery (Wh) and V_c is the volume of the catholyte (l).

The efficiencies of the batteries were calculated via the following equations:

$$\text{CE} = \frac{Q_{\text{discharge}}}{Q_{\text{charge}}} \times 100\% \quad (9)$$

$$\text{EE} = \frac{E_{\text{discharge}}}{E_{\text{charge}}} \times 100\% \quad (10)$$

$$\text{VE} = \frac{\text{EE}}{\text{CE}} \times 100\% \quad (11)$$

where $Q_{\text{discharge}}$ and Q_{charge} are the discharge capacity and charge capacity, $E_{\text{discharge}}$ and E_{charge} are the discharge energy and charge energy. Supplementary Tables 2–4 provide details.

Cadmium plating morphology

The plating morphology on the electrode was detected by scanning electron microscopy (JEOL JSM-7800F). Before testing, the anode plates, which were charged to a certain state, were freeze dried at -50°C .

Energy density calculation for comparison

The calculation of energy density E (Wh l^{-1}) in Fig. 1c was based on the discharge energy and volume of electrolyte on one side (zinc-iodine flow battery⁵, bromine- $\text{Li}_6(\text{P}_2\text{W}_{18}\text{O}_{62})$ flow battery (polyoxoanion)⁶, vanadium flow battery (VFB)³⁵) or the volume of solid active materials (LiFePO_4 , aq- LiMn_2O_4). The calculation of LiFePO_4 was based on the theoretical specific capacity of LiFePO_4 C (170 mAh g^{-1}) and battery voltage V ($3.2 \text{ V vs Li}^+/\text{Li}$); tap density ρ (1.0 g cm^{-3}) (ref. 36). The energy density of aqueous lithium-ion batteries (LiMn_2O_4) was mainly based on the $\text{LiMn}_2\text{O}_4\text{-VO}_2$ system. The theoretical specific capacity was -148 mAh g^{-1} , the voltage was -1.5 V and the tap density³⁷ reached 2.67 g cm^{-3} .

The energy density (Wh l^{-1}) of solid material was calculated as follows:

$$E = C \times V \times \rho \quad (12)$$

where C is the discharge capacity (mAh g^{-1}), V is the output voltage of the battery (V) and ρ is the tap density (g cm^{-3}).

Cost calculation

The theoretical cost of the positive redox species required per kWh was calculated as follows.

For a single electron transfer redox pair:

The specific capacity C (mAh g^{-1}):

$$C = \frac{F}{M_w} \times 1,000 \quad (13)$$

The cost per kWh U ($\text{US\$ kWh}^{-1}$):

$$U = \frac{U_m}{V \times C} \times 1,000 \quad (14)$$

where M_w is the molar weight of the redox species (g mol^{-1}), F is the Faraday constant (26.8 Ah mol^{-1}), U_m is the unit price ($\text{US\$ kg}^{-1}$) and V is the system voltage (V).

For a multielectron transfer redox pair:

The specific capacity C (mAh g^{-1}):

$$C_1 = \frac{F \times N_1}{M_w} \times 1,000 \quad (15)$$

$$C_2 = \frac{F \times N_2}{M_w} \times 1,000 \quad (16)$$

$$C_3 = \frac{F \times N_3}{M_w} \times 1,000 \quad (17)$$

The cost per kWh U ($\text{US\$ kWh}^{-1}$):

$$U = \frac{U_m}{V_1 \times C_1 + V_2 \times C_2 + V_3 \times C_3} \times 1,000 \quad (18)$$

where M_w is the molar weight of the redox species (g mol^{-1}) (for example, for IBA electrolyte is the molecular weight of iodide and bromide, treating the two components as a whole), F is the Faraday constant (26.8 Ah mol^{-1}), N is the electron transfer number (N_1 , N_2 and N_3 represent the number of electron transfers of each step), U_m is the unit price ($\text{US\$ kg}^{-1}$) (for IBA electrolyte, U_m is the price of iodide and bromide mixture per kg) and V is the system voltage (V) (V_1 , V_2 and V_3 represent the voltage of each step).

DFT calculation

The ESP and binding energy were calculated using density functional theory (DFT) in the Gaussian 16 package³⁸. The structures were optimized with the B3LYP³⁹ hybrid functional with the Def2-TZVP⁴⁰ basis set including the atom-pairwise dispersion correction (DFT-D3)^{41,42} with Becke–Johnson damping⁴³. The implicit universal solvation model based on solute electron density⁴⁴ was applied during the structure optimization. The optimized structures were checked by vibrational frequency analysis at the same calculation level to ensure that they were on the local minima of the potential energy surface. The ESP was analysed by the Multiwfn⁴⁵ package and was drawn by the VMD⁴⁶ package. The binding energy (E_{binding}) was calculated by the following equation.

$$E_{\text{binding}} = E(\text{H}_2\text{O} - B) - E(\text{H}_2\text{O}) - E(B) \quad (19)$$

where E represents the electronic energy of the component. B represents I_2 or IBr .

The absorption of I_2 and IBr on the carbon electrode was carried out by means of the Vienna Ab initio Simulation Package⁴⁷ with the projector-augmented wave⁴⁸ method. All calculations were based on the same generalized gradient approximation⁴⁹ method. The Perdew–Burke–Ernzerhof (PBE)⁵⁰ functional was applied to deal with the exchange-correlation term. Van der Waals interactions were accounted for at the DFT-D3^{41,42} with Becke–Johnson⁴³ damping level. The plane wave cut-off was set to 500 eV. Brillouin zone integration was carried out with a $2 \times 2 \times 1$ gamma point. The convergence thresholds for energy were set as 10^{-5} eV during ion relaxation, and the convergence thresholds for force were set as 0.02 eV \AA^{-1} . Charge density differences were analysed by means of the Vaspkit⁵¹ package.

Data availability

All relevant data are included in the paper and its Supplementary Information. Source data are provided with this paper.

References

- Xue, W. et al. Gravimetric and volumetric energy densities of lithium-sulfur batteries. *Curr. Opin. Electrochem.* **6**, 92–99 (2017).
- Liu, K., Liu, Y., Lin, D., Pei, A. & Cui, Y. Materials for lithium-ion battery safety. *Sci. Adv.* **4**, eaas9820 (2018).
- Anpo, M. et al. Safety analysis of energy storage station based on DFMEA. *E3S Web Conf.* **236**, 01006 (2021).
- Li, Z. & Lu, Y. C. Material design of aqueous redox flow batteries: fundamental challenges and mitigation strategies. *Adv. Mater.* **32**, e2002132 (2020).
- Weng, G.-M., Li, Z., Cong, G., Zhou, Y. & Lu, Y.-C. Unlocking the capacity of iodide for high-energy-density zinc/polyiodide and lithium/polyiodide redox flow batteries. *Energy Environ. Sci.* **10**, 735–741 (2017).
- Chen, J. J., Symes, M. D. & Cronin, L. Highly reduced and protonated aqueous solutions of $[P_2W_{16}O_{62}]^{6-}$ for on-demand hydrogen generation and energy storage. *Nat. Chem.* **10**, 1042–1047 (2018).
- Luo, J., Hu, B., Debruler, C. & Liu, T. L. A π -conjugation extended viologen as a two-electron storage anolyte for total organic aqueous redox flow batteries. *Angew. Chem. Int. Ed.* **57**, 231–235 (2018).
- Huskinson, B. et al. A metal-free organic-inorganic aqueous flow battery. *Nature* **505**, 195–198 (2014).
- Xie, C., Zhang, H., Xu, W., Wang, W. & Li, X. A long cycle life, self-healing zinc-iodine flow battery with high power density. *Angew. Chem. Int. Ed.* **57**, 11171–11176 (2018).
- Park, K. Y. et al. Concurrently approaching volumetric and specific capacity limits of lithium battery cathodes via conformal pickering emulsion graphene coatings. *Adv. Energy Mater.* **10**, 2001216 (2020).
- Nitta, N., Wu, F., Lee, J. T. & Yushin, G. Li-ion battery materials: present and future. *Mater. Today* **18**, 252–264 (2015).
- Wang, R., Cui, W., Chu, F. & Wu, F. Lithium metal anodes: present and future. *J. Energy Chem.* **48**, 145–159 (2020).
- Kolthoff, I. & Jordan, J. Amperometric titration and voltammetric determination of iodide. *Anal. Chem.* **25**, 1833–1837 (1953).
- Raspi, G., Pergola, F. & Guidelli, R. Electrooxidation of iodine on smooth platinum in aqueous media. *Anal. Chem.* **44**, 472–479 (2002).
- Zou, Y. et al. A four-electron Zn-I₂ aqueous battery enabled by reversible I^{(-)/I⁽⁰⁾}/I⁽⁺⁾ conversion. *Nat. Commun.* **12**, 170 (2021).
- Badea, G. E. Autocatalytic reduction of iodate at the platinum electrode in 0.5 M H₂SO₄ solutions. *Rev. Roum. Chim.* **52**, 491–498 (2007).
- Beran, P. & Bruckenstein, S. Rotating-disk-electrode study of the catalytic wave produced by the reduction of iodine in the presence of iodate. *J. Phys. Chem.* **72**, 3630–3635 (1968).
- Modestov, A., Andreev, V. & Antipov, A. Aluminum/bromate and aluminum/iodate mechanically rechargeable batteries. *Batteries* **8**, 270 (2022).
- Beran, P. & Bruckenstein, S. Voltammetry of iodine(I) chloride, iodine, and iodate at rotated platinum disk and ring-disk electrodes. *Anal. Chem.* **40**, 1044–1051 (2002).
- Hausmann, D., Koppe, R., Wolf, S., Roesky, P. W. & Feldmann, C. Ionic-liquid-assisted synthesis of the phosphorus interhalides $[PBr_4][I_2]$ and $[PBr_4][I_5Br]$. *Dalton Trans.* **45**, 16526–16532 (2016).
- Boyle, P. D. et al. Further structural motifs from the reactions of thioamides with diiodine and the interhalogens iodine monobromide and iodine monochloride: an FT-Raman and crystallographic study. *J. Chem. Soc. Dalton Trans.* **18**, 3106–3112 (2000).
- Aragoni, M. C. et al. DFT calculations, structural and spectroscopic studies on the products formed between IBr and N,N'-dimethylbenzoimidazole-2(3H)-thione and -2(3H)-selone. *Dalton Trans.* **13**, 2252–2258 (2005).
- Bichsel, Y. & von Gunten, U. Determination of iodide and iodate by ion chromatography with postcolumn reaction and UV/visible detection. *Anal. Chem.* **71**, 34–38 (1999).
- Jerman, I. et al. Ionic conductivity, infrared and Raman spectroscopic studies of 1-methyl-3-propylimidazolium iodide ionic liquid with added iodine. *Electrochim. Acta* **53**, 2281–2288 (2008).
- Favre, P., Jayasooriya, U. A. & Powell, D. B. Resonance Raman investigation of iodine and bromine adsorbed on porous vycor glass. *J. Raman Spectrosc.* **18**, 133–135 (1987).
- Li, B. et al. Ambipolar zinc-polyiodide electrolyte for a high-energy density aqueous redox flow battery. *Nat. Commun.* **6**, 6303 (2015).
- An, Y. et al. Synthesis, structure and characterization of $M(IO_3)_2(HIO_3)$ ($M = Ca, Sr$) as new anhydrous alkaline earth metal bis-iodate hydrogeniodate compounds. *Dalton Trans.* **48**, 13074–13080 (2019).
- Bushiri, M. J., Kochuthresia, T. C., Vaidyan, V. K. & Gautier-Luneau, I. Raman scattering structural studies of nonlinear optical $M(IO_3)_3$ ($M = Fe, Ga, \alpha\text{-In}$) and linear optical $\beta\text{-In}(IO_3)_3$. *J. Nonlinear Opt. Phys. Mater.* **23**, 1450039 (2014).
- Li, X., Xie, C., Li, T., Zhang, Y. & Li, X. Low-cost titanium-bromine flow battery with ultrahigh cycle stability for grid-scale energy storage. *Adv. Mater.* **32**, 2005036 (2020).
- Sonnenberg, K., Mann, L., Redeker, F. A., Schmidt, B. & Riedel, S. Polyhalogen and polyinterhalogen anions from fluorine to iodine. *Angew. Chem. Int. Ed.* **59**, 5464–5493 (2020).
- Easton, M. E. et al. The formation of high-order polybromides in a room-temperature ionic liquid: from monoanions ($[Br_5^-]$ to $[Br_{11}^-]$) to the isolation of $[PC_{16}H_{36}]_2[Br_{24}]$ as determined by van der Waals bonding radii. *Chem. A Eur. J.* **21**, 2961–2965 (2015).
- Lee, Y. et al. An organic imidazolium derivative additive inducing fast and highly reversible redox reactions in zinc-bromine flow batteries. *J. Power Sources* **547**, 232007 (2022).
- Ma, W. et al. High-performance solar redox flow battery toward efficient overall splitting of hydrogen sulfide. *ACS Energy Lett.* **5**, 597–603 (2019).
- Xie, C., Liu, Y., Lu, W., Zhang, H. & Li, X. Highly stable zinc-iodine single flow batteries with super high energy density for stationary energy storage. *Energy Environ. Sci.* **12**, 1834–1839 (2019).
- Wei, X. et al. Materials and systems for organic redox flow batteries: status and challenges. *ACS Energy Lett.* **2**, 2187–2204 (2017).
- Jin, Y. et al. High-tap density LiFePO₄ microsphere developed by combined computational and experimental approaches. *Cryst. Eng. Comm.* **20**, 6695–6703 (2018).
- Guo, D. et al. Electrochemical performance of solid sphere spinel LiMn₂O₄ with high tap density synthesized by porous spherical Mn₃O₄. *Electrochim. Acta* **123**, 254–259 (2014).
- Frisch, M. J. et al. Gaussian 16 Rev. A.03 (Gaussian Inc., 2016).
- Lee, C. T., Yang, W. T. & Parr, R. G. Development of the Colle-Salvetti correlation-energy formula into a functional of the electron density. *Phys. Rev. B* **37**, 785–789 (1988).
- Weigend, F. & Ahlrichs, R. Balanced basis sets of split valence, triple zeta valence and quadruple zeta valence quality for H to Rn: design and assessment of accuracy. *Phys. Chem. Chem. Phys.* **7**, 3297–3305 (2005).
- Grimme, S. Accurate description of van der Waals complexes by density functional theory including empirical corrections. *J. Comput. Chem.* **25**, 1463–1473 (2004).

42. Grimme, S. Density functional theory with London dispersion corrections. *Wiley Interdiscip. Rev.: Comput. Mol. Sci.* **1**, 211–228 (2011).
43. Johnson, E. R. & Becke, A. D. A post-Hartree-Fock model of intermolecular interactions: inclusion of higher-order corrections. *J. Chem. Phys.* **124**, 174104 (2006).
44. Marenich, A. V., Cramer, C. J. & Truhlar, D. G. Universal solvation model based on solute electron density and on a continuum model of the solvent defined by the bulk dielectric constant and atomic surface tensions. *J. Phys. Chem. B* **113**, 6378–6396 (2009).
45. Lu, T. & Chen, F. Multiwfn: a multifunctional wavefunction analyzer. *J. Comput. Chem.* **33**, 580–592 (2012).
46. Humphrey, W., Dalke, A. & Schulten, K. VMD: visual molecular dynamics. *J. Mol. Graphics* **14**, 33–38 (1996).
47. Kresse, G. & Furthmüller, J. Efficient iterative schemes for ab initio total-energy calculations using a plane-wave basis set. *Phys. Rev. B* **54**, 11169–11186 (1996).
48. Blöchl, P. E. Projector augmented-wave method. *Phys. Rev. B* **50**, 17953–17979 (1994).
49. Perdew, J. P., Burke, K. & Ernzerhof, M. Generalized gradient approximation made simple. *Phys. Rev. Lett.* **77**, 3865–3868 (1996).
50. Perdew, J. P., Ernzerhof, M. & Burke, K. Rationale for mixing exact exchange with density functional approximations. *J. Chem. Phys.* **105**, 9982–9985 (1996).
51. Wang, V., Xu, N., Liu, J.-C., Tang, G. & Geng, W.-T. VASPKIT: a user-friendly interface facilitating high-throughput computing and analysis using VASP code. *Comput. Phys. Commun.* **267**, 108033 (2021).
52. Qiao, L. et al. Highly stable titanium–manganese single flow batteries for stationary energy storage. *J. Mater. Chem. A* **9**, 12606–12611 (2021).
53. Chen, W. et al. A manganese–hydrogen battery with potential for grid-scale energy storage. *Nat. Energy* **3**, 428–435 (2018).
54. Liu, Y. et al. An aqueous redox flow battery with a tungsten-cobalt heteropolyacid as the electrolyte for both the anode and cathode. *Adv. Energy Mater.* **7**, 1601224 (2017).
55. Wang, C. et al. Cage-like porous carbon with superhigh activity and Br₂-complex-entrapping capability for bromine-based flow batteries. *Adv. Mater.* **29**, 1605815 (2017).
56. Liu, T., Wei, X., Nie, Z., Sprenkle, V. & Wang, W. A total organic aqueous redox flow battery employing a low cost and sustainable methyl viologen anolyte and 4-HO-TEMPO catholyte. *Adv. Energy Mater.* **6**, 1501449 (2016).
57. Xie, C., Duan, Y., Xu, W., Zhang, H. & Li, X. A low-cost neutral zinc-iron flow battery with high energy density for stationary energy storage. *Angew. Chem. Int. Ed.* **56**, 14953–14957 (2017).
58. Yuan, Z., Duan, Y., Liu, T., Zhang, H. & Li, X. Toward a low-cost alkaline zinc-iron flow battery with a polybenzimidazole custom membrane for stationary energy storage. *iScience* **3**, 40–49 (2018).
59. Luo, J., Hu, B., Hu, M., Wu, W. & Liu, T. L. An energy-dense, powerful, robust bipolar zinc-ferrocene redox-flow battery. *Angew. Chem. Int. Ed.* **61**, e202204030 (2022).
60. Yao, Y., Wang, Z., Li, Z. & Lu, Y. C. A dendrite-free tin anode for high-energy aqueous redox flow batteries. *Adv. Mater.* **33**, 2008095 (2021).
61. Zhang, J. et al. An all-aqueous redox flow battery with unprecedented energy density. *Energy Environ. Sci.* **11**, 2010–2015 (2018).
62. Li, Z., Weng, G., Zou, Q., Cong, G. & Lu, Y.-C. A high-energy and low-cost polysulfide/iodide redox flow battery. *Nano Energy* **30**, 283–292 (2016).
63. Xie, C. et al. A highly reversible neutral zinc/manganese battery for stationary energy storage. *Energy Environ. Sci.* **13**, 135–143 (2020).
64. Wang, C. et al. A TiN nanorod array 3D hierarchical composite electrode for ultrahigh-power-density bromine-based flow batteries. *Adv. Mater.* **31**, e1904690 (2019).

Acknowledgements

We thank Y. Xi at Dalian Institute of Chemical Physics for his support in battery test. This work was financially supported by National Natural Science Foundation of China (grant number 21925804, received by X.L., 22209179, received by C.X.), International Partnership Program of the Chinese Academy of Sciences (number 121421KYSB20210028, received by X.L.).

Author contributions

C.X. conceived the idea, performed the experiment and wrote the manuscript. Y.X. tested the performance of some batteries. In situ Raman test was performed by C.W. and Q.F. T.L. completed relevant theoretical calculations. X.L. supervised the work, discussed the results and revised the manuscript.

Competing interests

The authors declare no competing interests.

Additional information

Supplementary information The online version contains supplementary material available at <https://doi.org/10.1038/s41560-024-01515-9>.

Correspondence and requests for materials should be addressed to Xianfeng Li.

Peer review information *Nature Energy* thanks the anonymous reviewers for their contribution to the peer review of this work.

Reprints and permissions information is available at www.nature.com/reprints.

Publisher's note Springer Nature remains neutral with regard to jurisdictional claims in published maps and institutional affiliations.

Springer Nature or its licensor (e.g. a society or other partner) holds exclusive rights to this article under a publishing agreement with the author(s) or other rightsholder(s); author self-archiving of the accepted manuscript version of this article is solely governed by the terms of such publishing agreement and applicable law.

© The Author(s), under exclusive licence to Springer Nature Limited 2024